

Radar and Lightcurve Shape Model of Near-Earth Asteroid (1627) Ivar



Jenna L. Crowell^{a,*}, Ellen S. Howell^{b,c}, Christopher Magri^d, Michael C. Nolan^{b,c},
Yanga R. Fernández^a, James E. Richardson^{c,e}, Brian D. Warner^f, Sean E. Marshall^g,
Alessandra Springmann^b, Ronald J. Vervack Jr.^h

^aUniversity of Central Florida, Orlando, FL, USA

^bLPL/University of Arizona, Tucson, AZ, USA

^cArecibo Observatory, Arecibo, Puerto Rico

^dUniversity of Maine at Farmington, Farmington, ME, USA

^ePlanetary Science Institute, Tucson, AZ, USA

^fCenter for Solar System Studies - Palmer Divide Station, Rancho Cucamonga, CA, USA

^gCornell University, Ithaca, NY, USA

^hJohns Hopkins Applied Physics Laboratory, Laurel, MD, USA

ARTICLE INFO

Article history:

Received 12 May 2016

Revised 1 November 2016

Accepted 8 November 2016

Available online 19 November 2016

ABSTRACT

We present our shape model of Amor class near-Earth asteroid (1627) Ivar. During Ivar's apparition in 2013, in which it had a minimum distance of 0.32 AU, we obtained both CCD photometry and radar observations. The radar data consist of echo power spectra and delay-Doppler imaging with 300 m resolution and were obtained using the Arecibo Observatory's 2380 MHz radar. Lightcurve data were gathered using the 0.35 m telescope at the Palmer Divide Station. Using these data, we constructed a detailed shape model of Ivar that reveals more surface detail than earlier models. Ivar was found to have a rotational period of 4.7951689 ± 0.0000026 hours with a pole located within 6° of ecliptic longitude and latitude 336° and 37° respectively. Ivar is an elongated asteroid with maximum extensions along the three body-fixed coordinates being $15.15 \times 6.25 \times 5.66$ km $\pm 10\%$. The results of surface slope analysis suggest that Ivar is covered with a loose regolith. Ivar appears to reside in, or near, an optimum state with respect to its shape, spin, and bulk density, such that dynamic topography, surface slopes, and erosion rates on the body are near minimum levels and is therefore dynamically stable.

© 2016 Published by Elsevier Inc.

1. Introduction

Asteroid (1627) Ivar was discovered by Ejnar Hertzsprung in 1929 at the Leiden Southern Station in Johannesburg, South Africa. Ivar is an Amor class near-Earth asteroid (NEA) with an orbital semi-major axis of 1.863 AU and a perihelion distance of 1.124 AU. It is of taxonomic type Sqw, based on the combined visible and near-infrared spectrum in the Bus-DeMeo taxonomic system (DeMeo et al., 2009) and has an effective spherical diameter of approximately 8.485 km (Mainzer et al., 2014). Ivar was found to have a rotational period of 4.8 hours by Harris and Young (1986) and was more recently found to be 4.795 ± 0.002 hours by Warner (2015). In 1985, it became the first asteroid to be delay-Doppler imaged with radar by Ostro et al., (1990) who found it to have an irregular shape with a length roughly twice its width. Using charge-coupled device (CCD) photometry, Kaasalainen et al., (2004) constructed a nonconvex shape model of Ivar, Fig. 1,

and inferred its dimensions to be in the proportions 2.5:1.3:1. Kaasalainen et al. incorporated lightcurves from Hahn et al. (1989), Hoffmann and Geyer (1990), Chernova et al. (1995) and Pravec et al., (1996). Many of these observations were also included in our shape modeling to ensure that our model was consistent with the older data and constrain Ivar's physical properties.

During Ivar's apparition in 2013, we had the opportunity to observe the asteroid again with the Arecibo Observatory planetary radar system and obtain additional CCD lightcurves (Warner, 2014). In this paper, we present a higher-resolution shape model of Ivar constructed by analyzing recent radar and lightcurve datasets. This improved shape model is a critical part of our ongoing project to understand the thermal behavior, surface composition, and surface heterogeneity of S-complex NEAs (Howell et al., 2015; Howell et al., 2016; Crowell et al., 2015; Crowell et al., 2016). To this end, we also observed Ivar using the NASA IRTF's SpeX instrument (Rayner et al., 2003) in the reflected and thermal regimes (0.8 – 4.1 μm) from early March through early November of 2013. These observations were made temporally close to the radar and lightcurve observations. We will therefore be able to sync the orientation

* Corresponding author.

E-mail address: jenlyjones@knights.ucf.edu (J.L. Crowell).

Table 1
2013 Radar observations.

Observing date (UT)	Type	Runs	Power (kW)	Receive time (UT)	RA (HH:MM:SS)	DEC (DD:MM:SS)	d (AU)	ψ (°)
12 June	CW	3	685	09:02:00–09:30:37	22:08:50	+06:26:12	0.3450	318–353
27 June	CW	2	699	08:30:07–08:46:11	23:20:56	+07:34:32	0.3245	305–326
	Delay-Doppler	9	660	08:56:55–10:28:35	23:21:08	+07:34:34	0.3245	339–87
28 June	CW	2	651, 685	08:46:29–09:05:47	23:25:41	+07:34:58	0.3239	328–352
	Delay-Doppler	7	642	09:16:44–10:26:48	23:25:50	+07:34:58	0.3239	6–86
04 July	CW	1	710	08:45:01–08:50:15	23:53:04	+07:26:31	0.3217	337–343
	Delay-Doppler	4	700	08:59:28–09:49:18	23:53:10	+07:26:27	0.3217	348–51

The table lists the radar data type; the range of transmitter power for delay-Doppler images; the number of runs conducted; the receive start - end time; right ascension and declination near mid-time of observation of Epoch J2000.0; the distance, d , of Ivar from the observer in AU; and the rotational phase coverage, ψ , in degrees.

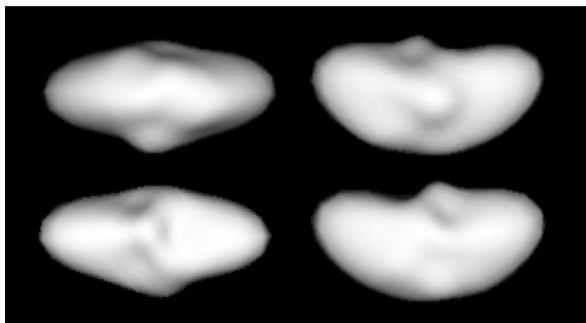


Fig. 1. Nonconvex shape model of Ivar produced by Kaasalainen et al. (2004) using lightcurves only and described as having a “somewhat banana-like appearance”.

of the asteroid to the near-IR observations using this new shape model, allowing us to infer surface properties of the asteroid. The infrared spectroscopy will be addressed in a future paper.

In the following section, we describe the photometry and radar observations used for the shape-modeling of Ivar and in Section 3, we describe our shape modeling software and the process used to create the final shape model. We discuss our results in Section 4 and our future plans are summarized in Section 5.

2. Observations

2.1. Radar data

Echo power spectra and delay-Doppler imaging were obtained with the Arecibo Observatory 2380 MHz planetary radar system in June and July of 2013. The procedure for acquiring radar data and the reduction methods we used are discussed in detail by Magri et al. (2007). The radar observing circumstances are shown in Table 1.

We obtained four days of continuous wave (CW) spectra during which monochromatic, circularly polarized, continuous signals were transmitted and the spectrum of received power versus frequency was measured. Both opposite (OC) and same circular (SC) polarizations echoes were recorded. The latter results from multiple scattering and is therefore usually weaker. Owing to this, we only incorporated the OC data into the shape-modeling for both the echo power spectra and the delay-Doppler images. These CW spectra help to constrain the size and rotation rate of the asteroid. By integrating the CW spectra, we calculate the radar albedo, i.e., the radar reflectivity of the surface. The ratio of the integrated SC and OC signal is the polarization ratio, which gives us information about the complexity of the surface on scales comparable to the radar wavelength. We discuss this further in Section 4.3.

We acquired three days of delay-Doppler images. For these runs, we apply a pseudo-random phase code to the signal to resolve the signal in both Doppler frequency and in range. The images were taken with a baud length of 2 μ s, which is equivalent

to 300 m resolution in range. For comparison, images recorded by Ostro et al. (1990) had a resolution of 1.2 km. In addition to providing further constraints on the size and rotation of Ivar, these delay-Doppler images reveal surface features in unprecedented detail. The rotational phase coverage of these observations allows us to resolve the delay-Doppler north/south ambiguity (Hudson & Ostro, 1994). Subradar latitudes covered range from 28° to 41°, which is similar to those covered by Ostro et al. (38°–40°). In Fig. 2, we show radar images and CW spectra taken on July 4, 2013. Similar to the results of Ostro et al., we see that Ivar appears to have 2 lobes, indicated by the arrows in panels B, C, and D.

2.2. Lightcurve data

CCD lightcurves were collected between early June and early October of 2013 using the 0.35 m f/9.1 Schmidt-Cassegrain Telescope and a FLI 1001E camera at the Palmer Divide Station (Warner, 2014). In order to improve the accuracy and precision of the known spin-period and pole position, we also included lightcurves dating back to 1985 (Hahn et al., 1989; Chernova et al., 1992; Hoffmann & Geyer 1990; Pravec et al., 1996; Skiff et al., 2012) in the later stages of the shape-modeling process. The lightcurve observational circumstances are listed in Table 2. For all lightcurves used, errors were estimated from the average offsets (in magnitude) for individual data points from a spline fit. These lightcurves are shown, along with the lightcurves produced by our best shape model, in Section 4.2. More recent lightcurves from the Palmer Divide Station also exist (obtained in 2015), and, although they were not used in creating the final shape model, they were used as an independent check of our model.

The plethora of photometry that is incorporated into the shape-modeling process also helps us to create a high-resolution shape model even though the radar imaging may have weaker signal-to-noise ratios (SNR) than those of some asteroids previously studied using radar observations. Due to this, the shape model presented here has a resolution comparable to that of the delay-Doppler images.

3. Shape modeling

3.1. SHAPE

To model the shape of Ivar, we used the SHAPE code, which was developed by Hudson (1994) and considerably enhanced by Magri et al. (2007, 2011). SHAPE incorporates lightcurves, radar data, and ephemeris data (provided by Jet Propulsion Laboratory’s HORIZONS¹) and iterates to find a shape model that best fits the observations. SHAPE has many free parameters and cycles through

¹ Jet Propulsion Laboratory HORIZONS Ephemeris Data: <http://ssd.jpl.nasa.gov/?horizons>.

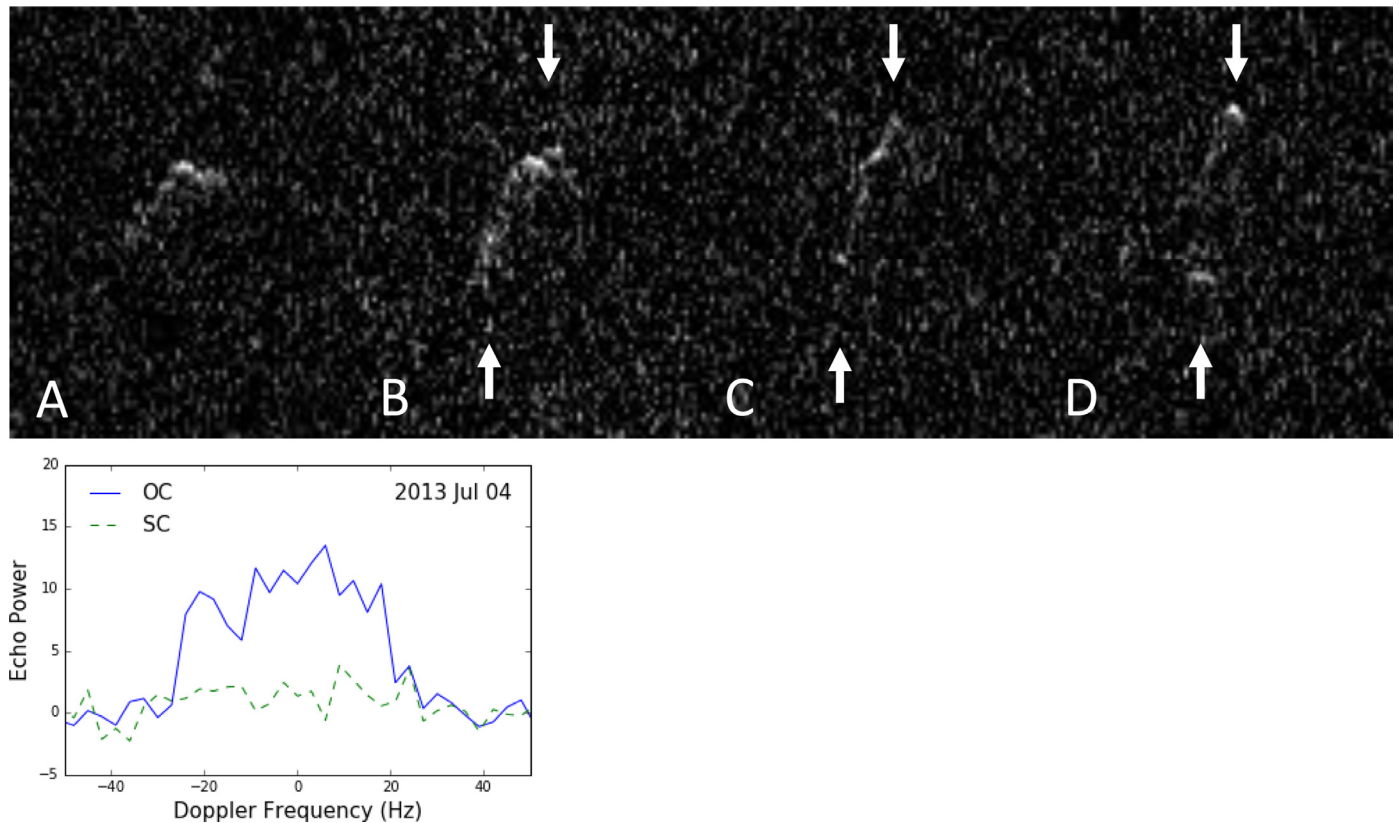


Fig. 2. In the top row, we show the delay-Doppler images taken on July 4, 2013. Panels A, B, C, and D indicate individual observations. The horizontal axis is Doppler shift while the vertical axis is the distance from the observer. To the left, we show the corresponding OC and SC spectra. The stronger OC spectra is represented by the solid line while the SC spectra is represented by the dashed line. These spectra have been binned to 3 Hz.

each one, allowing it to vary while holding the other parameters constant. It also allows for the use of penalty functions, which discourage heavily complex shape models. We generate synthetic lightcurves, delay-Doppler images, and radar spectra from the current shape model to compare with observed data. During an iteration, each vertex moves along a specified vector until a minimum in the objective function is found. The objective function is the absolute value of the observed minus the synthetic data, weighted by the user, combined with any specified penalty functions. This objective function is analogous to χ^2 , and is minimized to achieve the best-fit model. Other free parameters specify the model's spin state, its optical and radar scattering properties, and corrections to the radar observing ephemeris.

3.2. Shape-modeling process

The details of the general shape-modeling procedure are discussed by Magri et al. (2007, 2011), but here we summarize the procedure used for modeling Ivar. To reduce the overall computation time, we started with the shape model of Ivar produced by Kaasalainen et al. (2004), obtained from the Database of Asteroid Models from Inversion Techniques, DAMIT² (Durech et al., 2010). This model was converted to a polyhedron with 4800 vertices and 9596 triangular facets, giving this vertex model an average facet edge length of 270 m. A Hapke scattering law was used to model the optical properties of Ivar, with the Hapke parameters being derived from the albedo and phase darkening parameter G (Delbo et al., 2003; Tedesco et al., 1990). From JPL/HORIZONS, we

set $H=13.2$ and $G=0.60$, and we treated the surface scattering properties as being homogenous. For the radar scattering law, we used the 'cosine law', $\frac{d\sigma}{dA} = R(C+1)\cos^{2C}\Theta$, where Θ is the scattering angle, R is the Fresnel reflectivity at normal incidence and C is related to the r.m.s slope angle (Mitchell et al., 1996).

The pole coordinates and spin rate were initially set to those published by Kaasalainen et al. (2004). At this stage, SHAPE was not allowed to shift the positions of individual vertices, but could only vary three scaling factors that simultaneously expanded or contracted the entire model along each of the three body-fixed axes. Next, we "froze" the shape of this rescaled model and searched for an improved spin vector, as will be described in Section 4.1. Once we obtained spin parameters that provided the best fit to the data for this model, we allowed SHAPE to move individual vertices. This process of adjusting the vertices was carried out over several iterations.

Because some data have stronger SNRs and/or may exhibit more features that we hope to match, higher weights are assigned to what may be considered "better" datasets. This is especially important in minimizing the impact of radar images that exhibit high scatter and weak return signal. These weights adjust each dataset's contribution to the χ^2 value in the fitting process, thus making better datasets count more towards the final solution. Note that in a few of the radar images taken on June 28, we see signal from one end of the asteroid near the bottom of the images (discussed in Section 4.2). This feature proved difficult to model; therefore, a few of these images were given larger weights despite their low SNR to aid in reproducing this feature. Ultimately, we were forced to directly manipulate the shape model as, even with higher weight, we were unable to reproduce this particular feature of the radar images using SHAPE alone.

² Database of Asteroid Models from Inversion Techniques: <http://astro.troja.mff.cuni.cz/projects/damit>.

Table 2
Lightcurve observations.

Observing date (UT)	t (HH:MM)	Δt (h)	RA (HH:MM:SS)	DEC (DD:MM:SS)	m_v	d (AU)	ϕ (°)	Observer
12 Jun 1985	07:32:31	3.3	20:41:53	+09:54:16	11.71	0.2563	47.97	Young, J.W.
13 Jun 1985	06:47	4.9	20:46:22	+10:02:34	11.69	0.2530	48.24	Young, J.W.
12 Jul 1985	07:00	4.7	23:11:59	+07:37:49	11.23	0.2014	53.33	Harris, Belkora, Fico
14 Aug 1985	06:43	5.5	01:06:06	-06:46:08	11.35	0.2283	43.12	Harris, Belkora, Fico
31 Aug 1985	04:09	6.0	01:22:39	-13:52:27	11.54	0.2649	32.42	Di Martino
16 Sep 1985	04:06	5.6	01:18:16	-18:28:50	11.85	0.3168	22.64	Hahn, G.
18 Sep 1985	05:38	3.7	01:16:48	-18:51:41	11.90	0.3249	21.66	Hahn, G.
21 Sep 1985	05:32	6.7	01:14:24	-19:20:58	11.98	0.3381	20.37	Young, J.W.
27 Sep 1985	04:16	4.9	01:09:19	-19:56:44	12.17	0.3664	18.62	Hahn, Debehogne
16 Oct 1985	04:41	4.5	00:54:39	-19:18:31	12.96	0.4857	19.77	Young, J.W.
11 May 1990	18:40	1.9	14:10:16	+13:43:14	13.10	0.4986	23.88	Chernova, G.P.
13 May 1990	20:22	2.3	14:07:44	+14:01:44	13.09	0.4936	25.34	Chernova, G.P.
13 May 1990	22:29	2.5	14:07:40	+14:02:08	13.09	0.4935	25.37	Hoffman,Geyer
17 May 1990	22:19	2.8	14:03:07	+14:29:00	13.08	0.4854	28.17	Hoffman,Geyer
22 Jun 1990	19:37	2.7	13:51:38	+10:35:52	13.15	0.4538	50.60	Chernova, G.P.
23 Jun 1990	17:39	2.2	13:52:13	+10:20:10	13.15	0.4532	51.04	Chernova, G.P.
23 Feb 1995	11:31	2.8	13:14:08	+03:03:45	15.58	1.1670	19.38	Pravec, P.
01 Mar 1995	11:04	4.9	13:13:21	+04:04:59	15.37	1.0962	17.18	Pravec, P.
06 Mar 1995	10:34	5.7	13:11:40	+05:03:45	15.19	1.0426	15.14	Pravec, P.
05 Sep 2008	08:39	3.9	04:04:19	+07:17:14	14.50	0.8219	43.48	Koehn, B.W.
02 Oct 2008	07:34	4.8	04:13:28	+03:43:27	14.38	0.7684	31.09	Koehn, B.W.
07 Dec 2008	02:36	6.2	02:56:02	+00:51:22	15.19	1.0376	17.80	Koehn, B.W.
28 Jan 2009	02:43	2.8	03:07:60	+08:24:37	16.78	1.7723	26.93	Sanborn, J.J.
29 Jan 2009	02:47	2.6	03:08:55	+08:33:58	16.81	1.7883	26.94	Koehn, B.W.
01 Jun 2013	08:16	3.2	21:16:51	+04:31:27	12.74	0.3752	55.38	Warner, B.D.
02 Jun 2013	08:26	3.0	21:21:29	+04:43:39	12.72	0.3718	55.70	Warner, B.D.
03 Jun 2013	08:19	3.1	21:26:07	+04:55:28	12.71	0.3687	56.03	Warner, B.D.
20 Jun 2013	09:46	1.6	22:47:52	+07:17:04	12.53	0.3313	60.80	Warner, B.D.
22 Jun 2013	08:53	2.6	22:57:26	+07:24:36	12.52	0.3289	61.21	Warner, B.D.
14 Aug 2013	08:27	3.3	02:04:08	+00:01:51	12.50	0.3470	51.97	Warner, B.D.
15 Aug 2013	08:35	3.6	02:05:51	-00:14:43	12.50	0.3480	51.44	Warner, B.D.
16 Aug 2013	08:35	3.6	02:07:29	-00:31:25	12.50	0.3490	50.90	Warner, B.D.
05 Oct 2013	06:00	5.6	02:01:50	-13:18:53	12.75	0.4547	18.13	Warner, B.D.
02 Jan 2015	08:14	5.5	10:22:22	+10:42:25	17.02	1.8186	17.66	Warner, B.D.
03 Jan 2015	08:22	5.5	10:22:08	+10:46:35	17.00	1.8061	17.39	Warner, B.D.
04 Jan 2015	08:36	5.3	10:21:51	+10:50:57	16.97	1.7937	17.11	Warner, B.D.
06 Jan 2015	07:57	5.9	10:21:13	+11:00:11	16.93	1.7698	16.53	Warner, B.D.
07 Jan 2015	08:32	5.4	10:20:51	+11:05:13	16.91	1.7579	16.23	Warner, B.D.

The table lists the observing date; the starting time of observing run in UT, t; the duration of the observation in hours, Δt ; RA and DEC as in Table 1; the apparent visual magnitude, m_v , from JPL's Horizons; the distance, d, of Ivar from the observer in AU; and the solar phase angle, ϕ , in degrees; and the observer.

3.3. Modeling surface detail

SHAPE must cope with two constraints as it tries to improve the model's shape. First, it cannot shift the position of a given vertex in an arbitrary direction but must move it along a particular vector, chosen to be normal to the model's surface or else normal to the surface of the best-fit ellipsoid. Second, it is restricted in how far it can move that vertex from the neighboring vertices because we avoid "spiky" models by employing a penalty function that suppresses small-scale roughness. As a result of these constraints, it is difficult to fit a shape model that is radically different than its starting shape. For example, SHAPE will struggle if it is asked to start from a sphere but end with an irregular, lobed object [a similar problem was explored in detail by Magri et al. (2011) when modeling (8567) 1996 HW1]. This difficulty was partially abated by starting with the Kaasalainen et al. (2004) model, which was already close to the overall shape of the asteroid though without pronounced concavities; however, we continued to fit some radar images poorly in which clearly evident features (e.g., large bumps) were not being modeled well.

To overcome this obstacle in the modeling process, we incorporated the software Blender.³ Blender is a free, open-source code to model, render, and animate 3D objects and scenes. Blender allowed us to import the shape model produced by SHAPE and

manipulate vertices directly in order to create features that we could see in the images. This meant that we had to have a clear interpretation of the radar images in order to add features in the correct locations of the asteroid. Once we changed the model in Blender, we input it back into SHAPE and re-ran the fitting routine. This essentially gave SHAPE a new starting point at which to find a minimum in χ^2 .

It is important to note that, although we were free to directly mold the model, we generated the final shape models based on both the radar and lightcurve data in a consistent way using the SHAPE fitting algorithm. Manually editing the model with Blender ensured that the model SHAPE was working with was closer to the true shape of Ivar with each iteration, and, more importantly, it allowed us to avoid being stuck in local minima in χ^2 space. To guarantee that we did not end up with vertices spread too far apart after editing in Blender, we redistributed the vertices evenly along the surface of the model so that we did not unwittingly impose more constraints on vertex movement. We have run multiple trials where this vector path is set to move along a vector normal to the surface or along vectors describing an ellipsoid in order to compare the results.

Once the shape model produced synthetic data that were good fits to the observed data, we conducted a final grid search along ecliptic longitude and latitude over a smaller region, within 5° around the accepted value, to find the best fit for the ecliptic pole location, a process which is described in Section 4.1. Finally, we

³ Blender software: <https://www.blender.org/>.

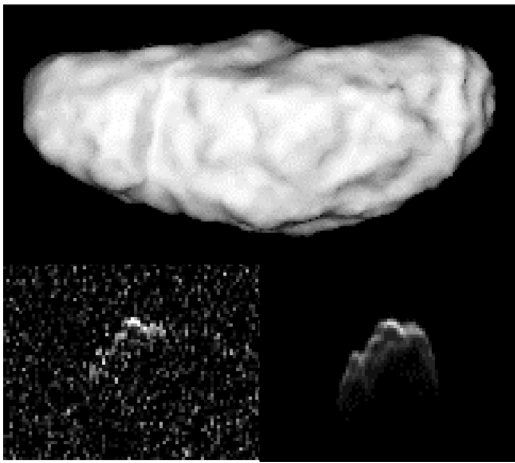


Fig. 3. A view of the model before smoothing looking in the +z direction (top), one of the radar images taken on July 4 (bottom left), and the synthetic radar from the model (bottom right).

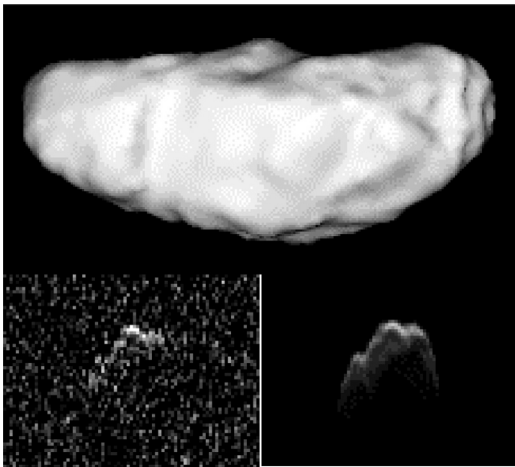


Fig. 4. A view of the model with all vertices smoothed. The image layout is the same as that in Fig. 3.

used a similar approach to determine the uncertainties in the X, Y, and Z dimensions in which we used a grid search employing the best-fit ecliptic pole coordinates.

3.4. Testing degree of smoothness

Because radar data are often relatively noisy, the resulting shape model often exhibits small-scale surface features that are due to fitting individual noise peaks rather than actual topography. Although the lightcurves were also incorporated into the shape-modeling, the radar images were given a higher weight because information about the surface structure is easier to untangle from the radar data, thus their contributions to reduced χ^2 were higher. By using Blender in the way that we describe here, we were able to tease out what features were both crucial to the radar image fits and what features had significant impacts on the fits to the lightcurves. In Figs. 3 and 4, we illustrate this effect of overfitting to radar imaging. In Fig. 3, the synthetic radar image matches well with the observed radar image, and the reduced χ^2 resulting from fitting both radar data and lightcurves is within an acceptable range. But whereas the large-scale topography originates with the strong features in the radar images, the smaller features are driven primarily by the noise in these data, giving the shape model a “lumpier” appearance than it is likely to have in reality.

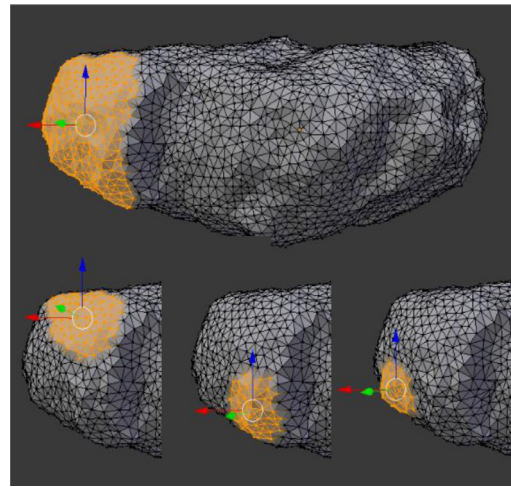


Fig. 5. Vertex groups in Blender. In the top image we show a large portion of the asteroid (in orange) selected for smoothing. In the event that any degree of smoothing such a large section provides a worse fit, the section is broken into smaller groups to be individually tested (bottom 3 panels). (For interpretation of the references to colour in this figure legend, the reader is referred to the web version of this article.)

Fig. 4 shows a model smoothed over the entire surface. There are subtle differences in the synthetic radar image from the rougher model shown in Fig. 3, but this smooth model yields nearly as good a fit to the radar data.

To investigate the level of surface topography that is represented by the observations, we altered the model by smoothing small areas across the surface and noting the changes in the fits to both the radar and lightcurve data. If the either of these fits were adversely affected, we rejected the change; if only a slight smoothing of the radar image resulted, with a sufficiently small effect on χ^2 , we accepted it. The goal of this smoothing investigation was to find the smoothest model that is as good as or better than the initial unsmoothed shape model in terms of reduced χ^2 .

This patchwise smoothing was accomplished using Blender to select regions on the rougher shape model containing areas of small-scale roughness that which, when altered, left prominent radar features in the synthetic images unchanged. Many individual patches were selected across the surface of the asteroid and tested at varying degrees of smoothness in an iterative process. Blender’s smoothing modifiers were used to explore the level of acceptable smoothness of the model. These modifiers employ a simple smoothing algorithm in which each new vertex position is calculated as the weighted average position of it and its neighboring vertices. The weighting is individually specified for each group of vertices selected to be smoothed. For each vertex group, we tested a range of weights for their effect on the fit to the radar data and the resulting reduced χ^2 for all lightcurves listed in Table 2.

Initially the smoothing was applied to the entire shape model; however, this resulted in fits that were worse than the unsmoothed model. Next, we selected large sections of the surface to test, but in many of these cases the quality of the fit was also worse, primarily because the fits to the lightcurves were poorer. We then tried smaller, individual sections along the surface in an effort to preserve small topography that may be required to match specific features in the data while still testing how a smoother surface affected the fits. As an example, Fig. 5 shows a case in which a larger area (top panel) was tried but the smoothing decreased the quality of the fit. This larger section was subsequently broken into smaller sections to be individually tested (bottom three panels in Fig. 5). This process was repeated over the entire surface of the asteroid and in each iteration, only those models

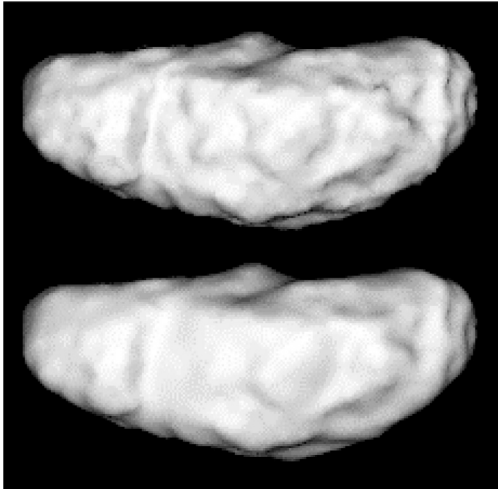


Fig. 6. The model before smoothing (top) compared to our final model (bottom) looking along the +z axis.

for which the smoothing lowered the reduced χ^2 were accepted. Once we completed this process over the entire asteroid, one final smoothing was applied to the whole surface to better blend the smoothed and unsmoothed sections. This slightly increased the reduced χ^2 , but the final value was still better than that for the unsmoothed model.

In Fig. 6, we show the model before smoothing (top) and the final model (bottom). It is important to note that although the final shape model may possess small bumps that result in a better fit to the lightcurve data, their actual location on the model surface is only representative of the topographic scales that affect the data. This final model is thus not a unique best fit to the data at these smaller scales. The larger topographic features, however, are required to fit the data and do reflect the bulk shape of the asteroid. This process proved more satisfactory than similar trials in which the smoothing penalty was increased because we could directly control the regions affected, rather than individual vertices.

4. Results and discussion

4.1. Spin rate and ecliptic pole

A reliable spin rate is needed to constrain the pole position because models with small differences in spin rate and axis dimensions can fit the radar images equally well. The extensive lightcurve data allowed us to determine the rotation rate with high accuracy. Using our model, we fit the 1985–2015 lightcurves and determine the sidereal rotation period of Ivar to be 4.7951689 ± 0.0000026 h, consistent with numerous reported spin rates of Ivar. The uncertainty given here is approximately 9 ms, and is effectively 1σ .

The pole solution in terms of ecliptic J2000.0 longitude and latitude is $336^\circ \pm 6^\circ$ and $+37^\circ \pm 6^\circ$, respectively. Our results are consistent with Kaasalainen et al. (2004), who found $+43^\circ$, $333^\circ \pm 10^\circ$. In order to find the best-fit solution to the poles, we used an iterative approach, described in detail by Nolan et al. (2013) and briefly described here. We first ran a series of models whose poles were held fixed at a series of sky positions defining a grid with 5° centered about $+43^\circ$, 333° covering $\pm 20^\circ$ in each direction. Using the results of this grid search to narrow down the sky region constraining the pole, we then ran a second grid search covering this smaller region with 2° resolution $\pm 10^\circ$ from the new minimum and finally with 1° resolution $\pm 5^\circ$ centered about the best fit. During these runs, we allowed SHAPE to vary the spin

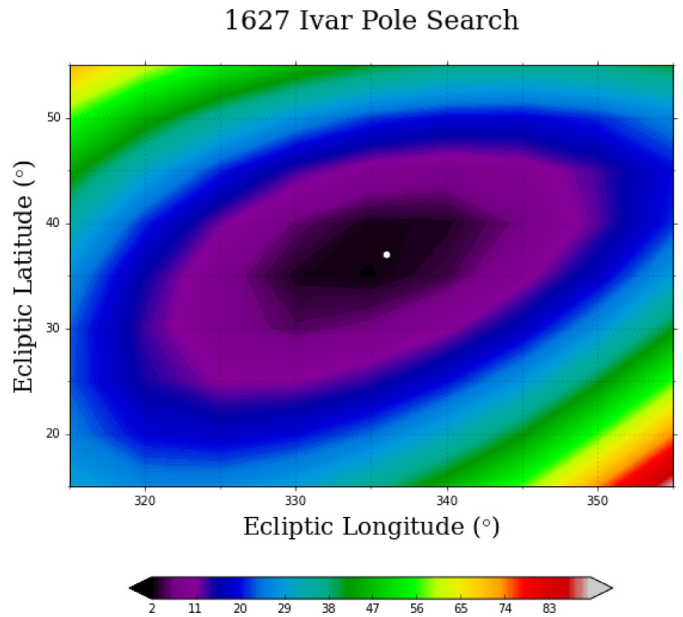


Fig. 7. Contour plot of the pole search, with the color bar representing reduced χ^2 values. The white dot represents the best-fit for the entire dataset listed in Table 2 located at 336° , $+37^\circ$.

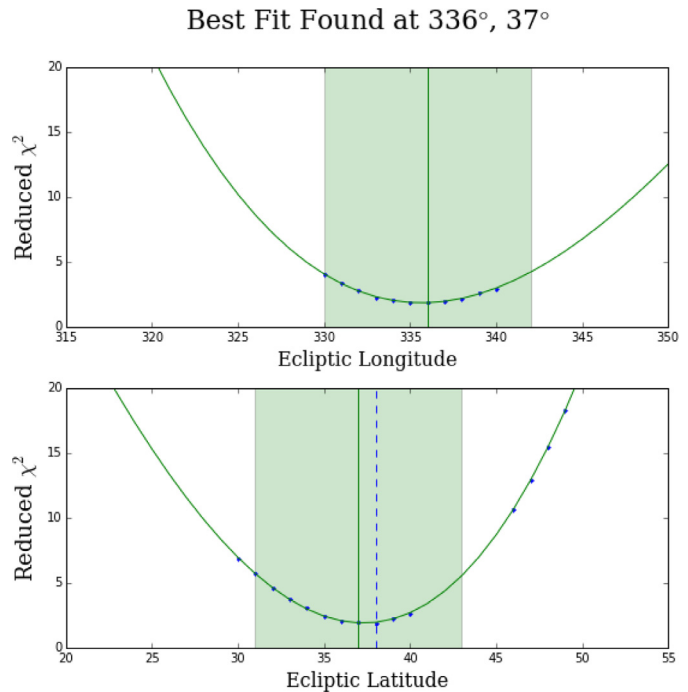


Fig. 8. Uncertainty analysis for ecliptic pole position: blue data points represent SHAPE fit trials and their resulting reduced χ^2 values, with the dashed blue line indicating the absolute smallest reduced χ^2 ; the green curve is the cubic fit to these data with the green vertical line marking the minimum. The distance in degrees that it takes reduced χ^2 to increase by 1 is taken to represent the 1σ uncertainty, which is shown in the green highlighted region. (For interpretation of the references to colour in this figure legend, the reader is referred to the web version of this article.)

rate, axes, and the rotation angle and only included lightcurve data as they impose the best constraints on the pole location. We show the results of this search in Fig. 7. For the uncertainty analysis, we plotted reduced χ^2 versus ecliptic longitude/latitude, shown in Fig. 8, and took 1σ to be the distance from the best fit to where

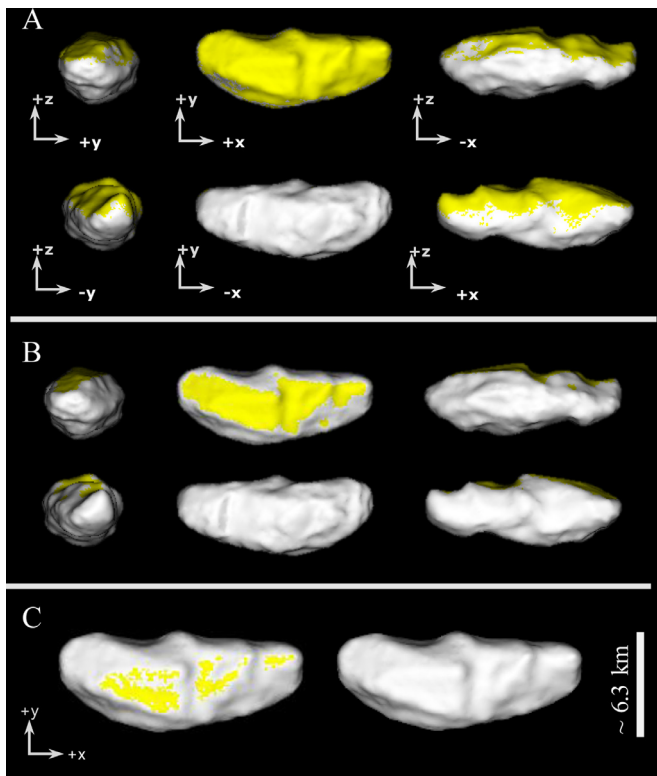


Fig. 9. Final shape model of Ivar. Panel A shows our model with areas unseen by the 2013 radar data marked in yellow. Panel B marks areas unseen by both 2013 radar and 2013 lightcurves. In Panel C, looking down the north pole, the left image has the 2008 and 2009 lightcurve data included and the image on the right includes all of the data listed in Tables 1 and 2, which give complete coverage. (For interpretation of the references to colour in this figure legend, the reader is referred to the web version of this article.)

this reduced χ^2 increased by one. Fig. 7 shows that the longitude and latitude uncertainties are correlated.

With an accurate spin rate and the ecliptic pole location, we could also investigate the limits for possible YORP effects. To test for this, we use SHAPE to define rates of change for the spin rate ($d\omega/dt$) and, integrating backwards, we look for the threshold for when we are unable to fit all of the lightcurves. Specifically, we search for a $d\omega/dt$ at which, by slightly adjusting the spin rate, we are able to match lightcurves from 2013 and 1985, but the fit to the lightcurves in 1995 are now visibly poor. We find that this limit occurs at a $d\omega/dt$ of ± 0.00000005 deg/day² and thus any possible acceleration is less than or equal to this value. For comparison, $5E-8$ deg/day² is about 60 times smaller than the YORP rate obtained by Kaasalainen et al. (2007) for 1862 Apollo which is 10 times smaller than Ivar in size.

4.2. Shape model

The final shape model of Ivar is shown in Fig. 9 and its properties are listed in Table 3. During 2013, much of one side of the asteroid was unseen, but the addition of the older lightcurves allows for more coverage in this region (Panel C). In Fig. 10, we demonstrate the match between the observed radar images and the synthetic ones produced by the model along with a sky view of the model during the mid-time of observation. Our final model is able to reproduce the radar data quite well.

To illustrate the overall improvement in the shape model, in Fig. 11, we compare our final model results to those using the Kaasalainen et al. (2004) model for a subset of the observations. In this figure, the spin and orientation settings for the Kaasalainen

Table 3
Properties of the shape model.

Dimensions along principal axis (km)	X	15.15 ± 10%
	Y	6.25 ± 10%
	Z	5.66 ± 10%
DEEVE (km)		15.38 × 5.80 × 4.93
Equivalent diameter of a sphere (km)		7.60 ± 10%
Area (km ²)		226.19 ± 20%
Volume (km ³)		230.05 ± 30%
Ratios of principal moments of inertia of a uniform-density	I_z/I_x	4.65 ± 20%
	I_z/I_y	1.04 ± 20%
Sidereal Period (h)		4.7951689 ± 0.0000026
Pole Ecliptic Longitude (°)		336 ± 6°
Pole Ecliptic Latitude (°)		+37 ± 6°

X, Y, and Z values correspond to the axes shown in Fig. 9. The dynamically equivalent equal-volume ellipsoid, DEEVE, parameters ($X \times Y \times Z$) have estimated uncertainties similar to the extents along principal axes values, with X, Y and Z values known within 10%. Italicized text gives the previous known values for comparison.

et al. model are the same as those in our model, but the size of the Kaasalainen et al. model was allowed to vary so that SHAPE could find the best match to the radar data; this produced a shape model that is slightly smaller than our model. Though the Kaasalainen et al. model does a good job fitting the overall shape, our model reproduces more of the asteroid's finer structure seen in the radar data.

In Fig. 12, we highlight the surface feature that was added to reproduce the 'bump' in the radar image, (discussed in Section 3.2). It is possible that this feature is not purely topographical, but perhaps there exists a spot on the surface that has a higher radar albedo.

In Fig. 9, looking down the +y axis, we see what appears to be a knuckle-like feature, not unlike what is seen on 4179 Toutatis (Huang et al., 2013) and 1620 Geographos (Hudson & Ostro, 1999). These comparisons are shown in Fig. 13. It is important to note that this side was not observed with radar and this feature is a result of fitting to our lightcurve data, as is illustrated in Fig. 9.

For the final shape model, we ran a series of fits around the best-fit pole location, allowing the vertices of the model to change, yielding the results shown here. We found Ivar to have maximum extents along the three body-fixed coordinate axes (Fig. 9) of $15.15 \times 6.25 \times 5.66$ km ± 10%. To find the 1σ uncertainty for each dimension, we fit the different scaling factors along the X, Y and Z dimensions separately. Because the ecliptic pole location and the spin rate are both well constrained (due to our extensive lightcurve dataset) and owing to our observing geometry, the CW spectra imposed the best constraint on the size of the X dimension. Because the CW spectra do not cover end-on orientations, lightcurves provided the best constraint for the Y and Z dimension. In Fig. 14, we show the fits to the OC CW spectra and the orientation at each observation. To test these dimensions, we changed the Y scale factor, increasing and decreasing in 5% increments. For each value of the Y scale factor, we allowed the Z dimension to vary, and kept X at the optimal dimension derived from the CW spectra and fit these to all of the lightcurves listed in Table 2. In the case of the X dimension, we took 1σ uncertainty to be where our minimum in reduced χ^2 increased by 1. For both Y and Z dimensions, the 1σ uncertainties were derived in the same way as for the ecliptic pole location. This degree of elongation is larger than what Ostro et al. suspected with

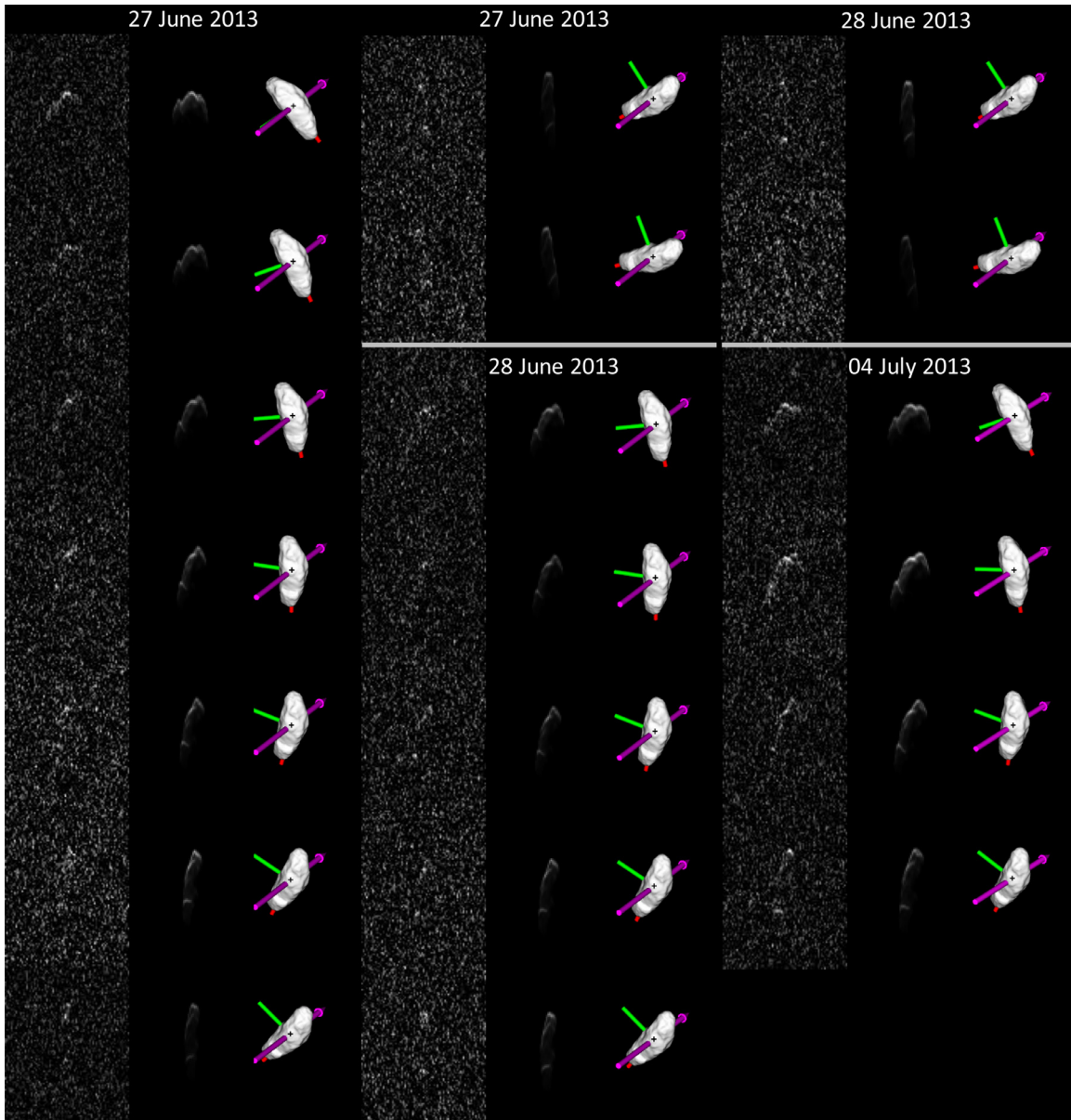


Fig. 10. The columns show, from left to right, the observed radar images, the synthetic radar images, and the corresponding sky view (as seen by the observer) of the shape model. In the sky view, we show the intermediate principal axis (green), the long principal axis (red), spin vector (magenta), and the center-of-mass marked by the '+'. (For interpretation of the references to colour in this figure legend, the reader is referred to the web version of this article.)

the maximum extent being approximately 12 km but they had assumed a nearly pole-on view during their observation because they did not have as many restrictions on the pole direction as our dataset provides. Ostro et al. emphasized that the estimated standard error did not consider the subradar latitude uncertainty. These reasons could explain the discrepancies in the maximum extent.

In Fig. 15, we show a few examples of the fits to lightcurves taken between 1985–2013. To see fits for all of the lightcurves included in this shape-modeling process, please see the supplemental material. As a final sanity-check of our model, we generated predictions for the 2015 CCD lightcurves (Warner et al., 2015), and demonstrate how well our model fits these lightcurves in Fig. 16. The uncertainties in the 2015 lightcurves are those given by Warner et al. These fits show that our shape model is consistent with the 2015 data.

4.3. Radar albedo and polarization ratio

Radar albedo indicates how reflective the surface is in radar compared to a perfect metal sphere, with values ranging from 0 to 1, where higher values show higher degrees of reflectivity. A high radar albedo could suggest the presence of metals on the surface. To calculate the OC and SC radar albedos, we integrated the OC and SC sense echo power spectra (see Fig. 17) to find the radar cross sections. The radar cross section is then divided by the geometric cross section, which is calculated using the model's projected area at the time each spectrum was acquired. The radar albedo is dominated by 25% systematic calibration uncertainty on the radar cross sections. We calculate the polarization ratios, μ_c , for each observation in order to infer the complexity of the surface on the wavelength scale. The error in μ_c is 5% because the systematic errors are the same for both $\hat{\sigma}_{sc}$ and $\hat{\sigma}_{oc}$ and therefore cancel. OC radar albedo, $\hat{\sigma}_{oc}$, and polarization ratios, $\hat{\sigma}_{sc} / \hat{\sigma}_{oc}$, are listed in

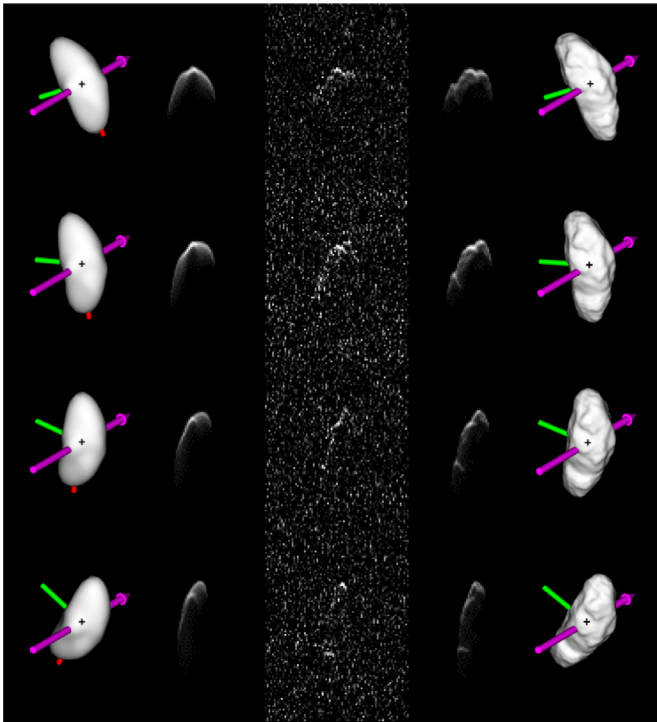


Fig. 11. This image compares the Kaasalainen et al., (2004) shape model (left) and our shape model (right), for data taken on July 4. Columns show the sky view of the Kaasalainen et al. model, the synthetic radar image that it produces, the observed radar image, the synthetic radar image produced with our model, and the sky view of our model.

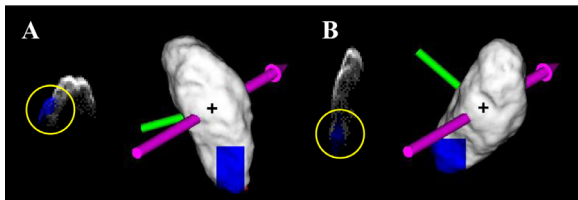


Fig. 12. In these two views of the shape model and associated synthetic radar image, the blue region is that which was initially edited in Blender in order to reproduce the observed radar feature that SHAPE struggled to reproduce. (For interpretation of the references to colour in this figure legend, the reader is referred to the web version of this article.)

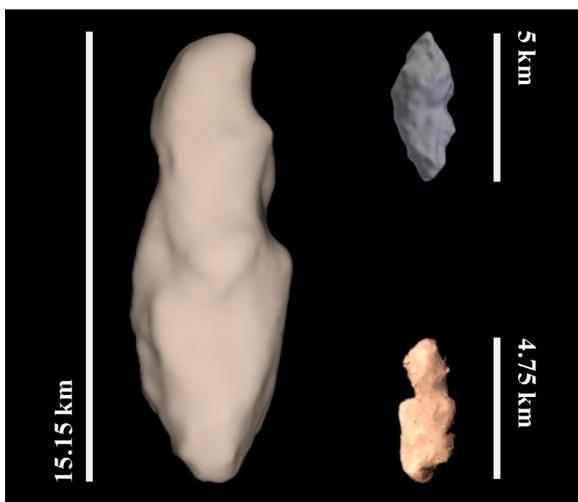


Fig. 13. Comparison of “knuckle” features: on the left, Ivar as viewed down the +y axis; on the top right, the shape model of Geographos; on the bottom right, the image of Toutatis taken by Chang’e 2. These features are oriented to the right side for each asteroid.

Table 4
OC radar albedo and polarization ratio.

Date	θ ($^\circ$)	$\hat{\sigma}_{oc}$	μ_c
12 June 2013	107	0.12	0.17
	122	0.12	0.19
	136	0.11	0.20
27 June 2013	60	0.12	0.35
	73	0.12	0.29
28 June 2013	81	0.18	0.22
	98	0.13	0.21
	83	0.15	0.20

Rotation phase angle relative to the zero point referred to in Section 3.2 is given by θ in degrees with corresponding sky images and CW spectra shown in Fig. 17. Uncertainties for the albedo values are 25%, and the circular polarization ratio is known to within 5%.

Table 4, which show Ivar to have an average $\hat{\sigma}_{oc}$ of 0.13 ± 0.03 ; this is in agreement with Ostro et al.’s results of 0.17 ± 0.04 . For comparison, Virkki et al. (2014) found that standard S type asteroids tend to have an $\hat{\sigma}_{oc}$ of 0.14 with a standard deviation of 0.046. This study had a sample size of 42 asteroids and was not limited to NEAs. The average polarization ratio for Ivar is 0.23 ± 0.01 , which is also consistent with Ostro et al.’s polarization ratio of 0.21 ± 0.01 .

4.4. Gravitational and surface properties

For the final shape model, we use the methods described by Richardson et al. (2014) to compute the combined gravitational and rotational potential, local acceleration, and surface slope experienced at the center of each facet, from which the dynamic elevation may be computed relative to other facets. Dynamic elevation h_{dyn} on a small Solar-System body was initially defined by Thomas (1993) as:

$$h_{dyn} = \frac{U_{local} - U_{mean}}{g_{local}},$$

where U_{mean} is the mean combined (gravitational + rotational) potential over the entire surface of the body, U_{local} is the combined potential at the center of the facet in question, and g_{local} is the combined acceleration at the center of the facet.

Gravitational potential and acceleration at each facet are computed using the surface-polyhedron gravity technique developed by Werner (1994). Using this method, the integration occurs over the surface area of the body (the number of facets). This method saves significant computation time and produces a better result than most volume integrators (Werner, 1994). The rotational potential and acceleration at the center of each surface facet are computed separately and combined with the gravitational results at the same surface location. This technique has been successfully applied in a number of previous studies, including by Richardson et al. (2007) and Richardson & Bowling (2014).

Assuming a bulk density of $\rho = 2500 \text{ kg m}^{-3}$, which is consistent with the S-type spectral class (Abe et al., 2006; Thomas et al., 1996; Yeomans et al., 2000), and a rotation period of 4.7952 h, Fig. 18 shows the shape model of Ivar color-coded according to dynamic elevation (left image in each pair) and surface slope (right image in each pair). The normalized surface distributions for these parameters are shown in Fig. 19 (left and middle plots). The vast majority of surface slopes on the body are at less than typical values of the angle-of-repose for geologic materials (about 30° – 35°). This strongly suggests the presence of a loose, relatively cohesionless regolith material covering most of the surface of the body, which is capable of gradually flowing downslope in response to such stimuli as impact-induced seismic shaking (Richardson et al., 2004, 2005).

As a further exercise, we next attempted to find Ivar’s ‘optimum’ bulk density that corresponds to its most eroded state

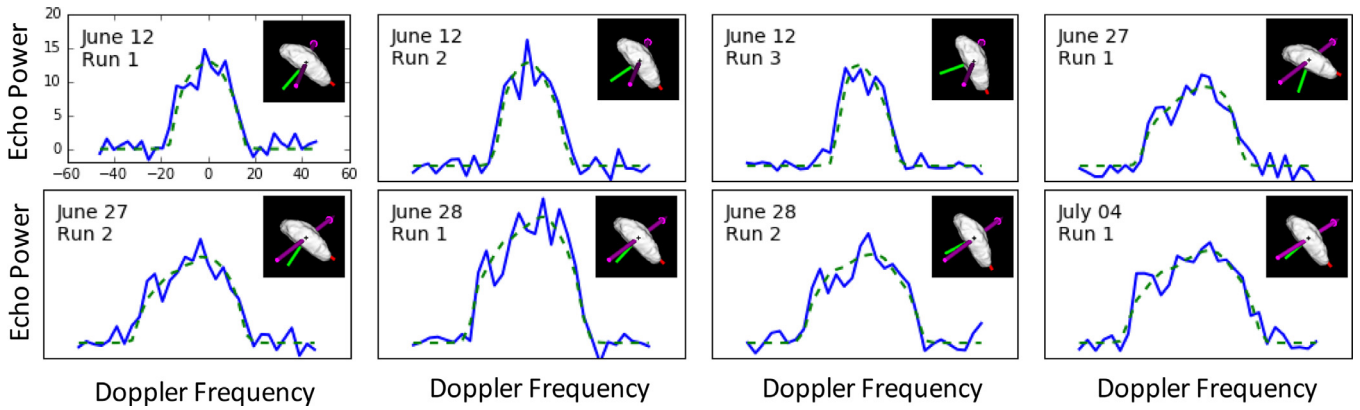


Fig. 14. The fit of the final shape model to the OC CW spectra, dashed line, with the observed spectra, solid line. Echo power, in units of standard deviations of the noise, is plotted vs. frequency in Hz. Data are shown in chronological order from left to right. The scales are identical in each plot and the bin width is ~ 3 Hz.

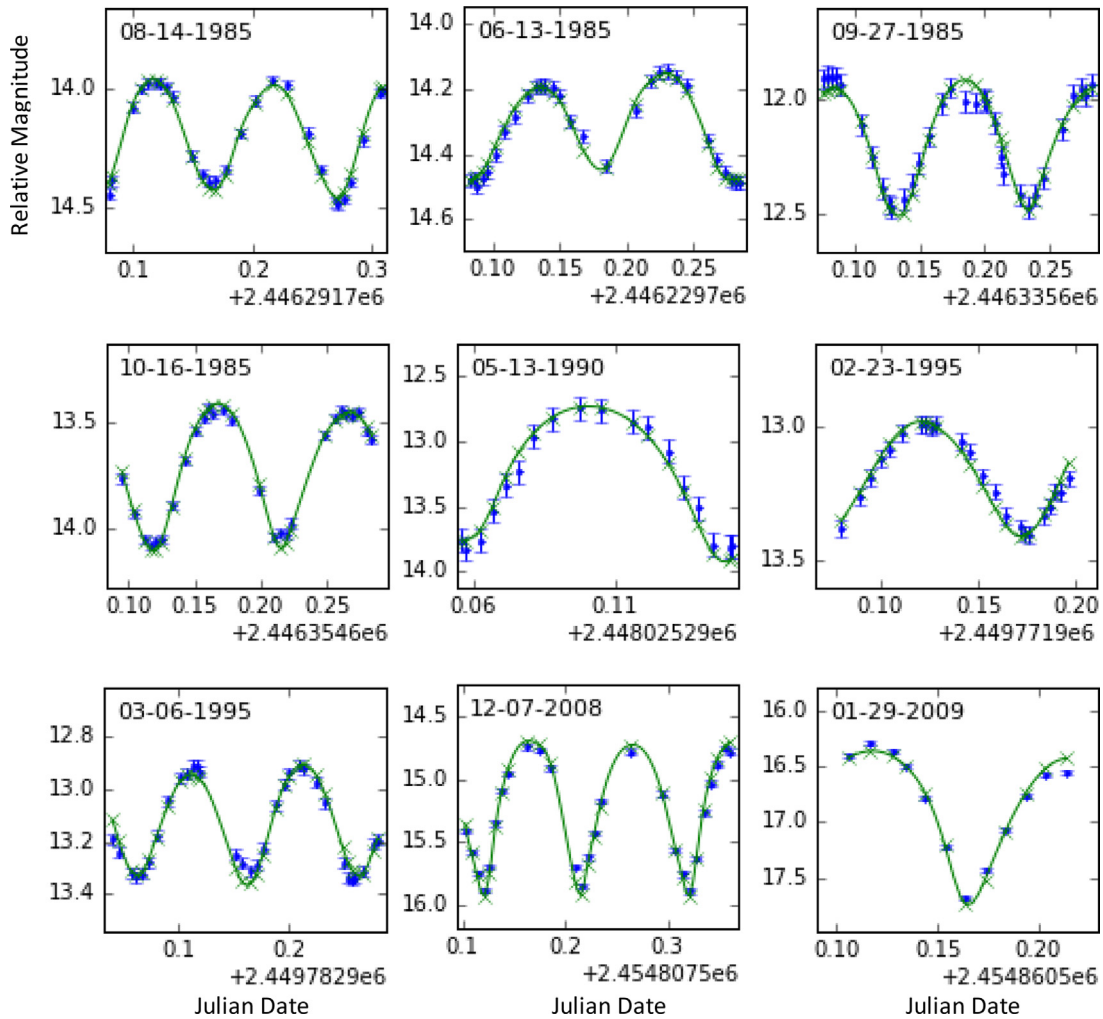


Fig. 15. Fits to the Ivar lightcurves assuming the final shape model. Relative magnitude is shown versus time in units of decimal days relative to the listed UT Julian date (MM-DD-YYYY). Observed lightcurve points are shown in blue; while the lightcurves generated by the model are shown in green. (For interpretation of the references to colour in this figure legend, the reader is referred to the web version of this article.)

(lowest elevation extremes and lowest slope distribution) given its current shape, spin state, and topography. The procedure, assumptions, and the arguments for why ‘optimum’ bulk density could be close to an object’s actual bulk density are presented by Richardson & Bowling (2014). The only difference is that we report here an uncertainty range based on the full-width at quarter-minimum (FWQM) technique rather than at half-minimum (see

Fig. 19, right panel). For Ivar, we find the optimum bulk density occurs at a value of $\rho = 2450$ (1700–4100) kg m^{-3} . This is consistent with the measured bulk density values of other S-type asteroids, such as 1950 ± 140 kg m^{-3} for near-Earth asteroid (25,143) Itokawa (Abe et al., 2006) and 2670 ± 30 kg m^{-3} for (433) Eros (Yeomans et al., 2000), both measured directly by near-proximity spacecraft radio-science observations. The implication is that Ivar currently

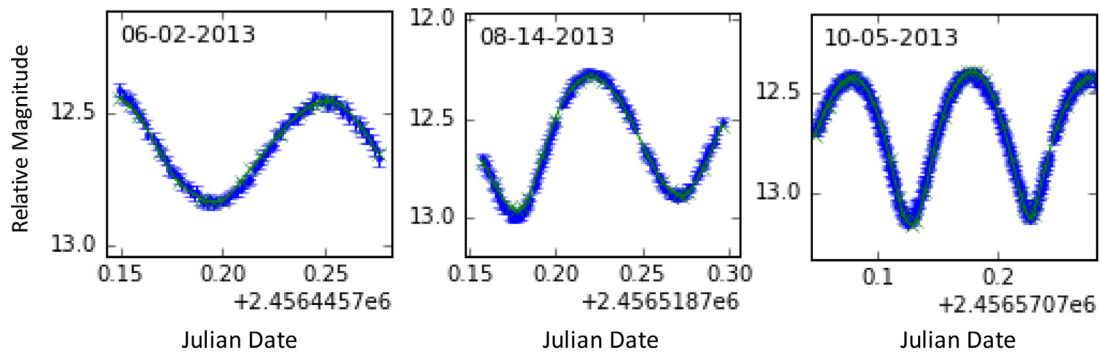


Figure 15. Ivar lightcurves and model. (Continued)

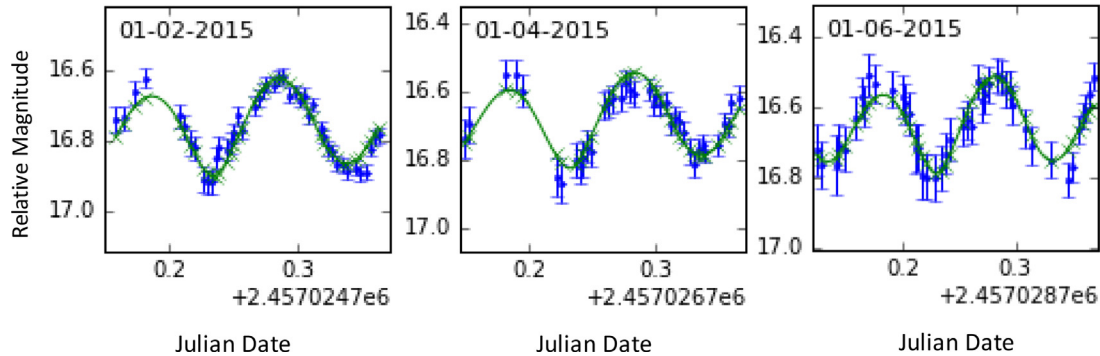


Fig. 16. Examples of 2015 predictions shown in the same format as in Fig. 15.

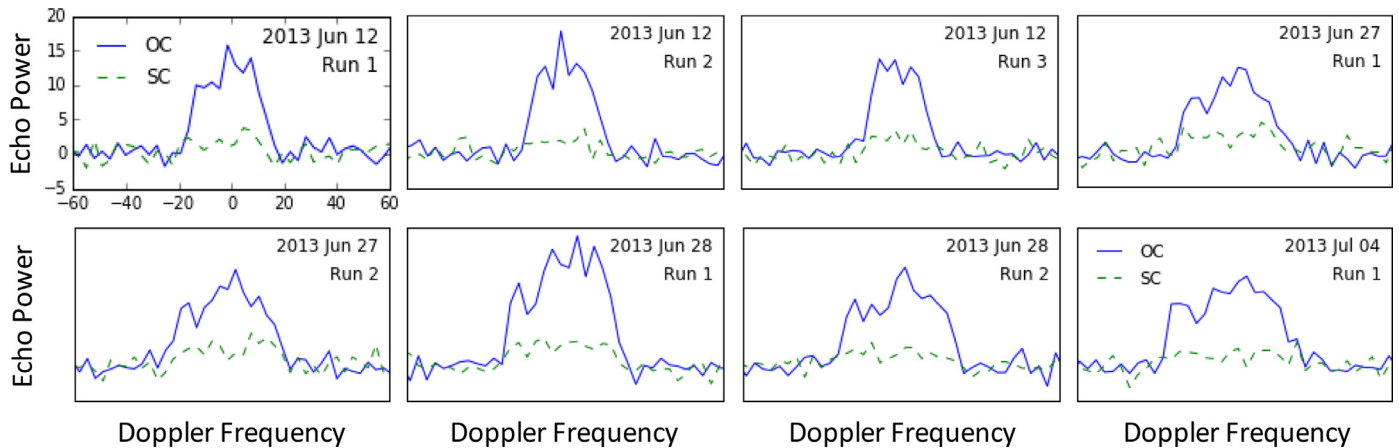


Fig. 17. Plots of OC and SC CW spectra. Echo power, in units of standard deviations of the noise, is plotted vs. frequency in Hz. The scales are identical in each plot and the resolution is approximately 3 Hz.

resides in or very near an optimum state with respect to its shape, spin, and bulk density, such that dynamic topography, surface slopes, and erosion rates on the body are near minimum levels. If the density is near to this value, it could mean that Ivar is more likely to have a "fractured monolith" type of internal structure (as defined in Britt et al. (2002)), similar to that assumed for 243 Ida at a density of $2600 \pm 500 \text{ kg m}^{-3}$ (Thomas et al., 1996) and Eros as opposed to a disaggregated and reassembled "rubble pile" type of internal structure.

5. Summary

By combining radar and lightcurve observations, we have derived a shape model of Ivar. Our delay-Doppler images, with a resolution of 300 m, enable us to model surface detail at a comparable scale. We have found Ivar to be more elongated than

in the model presented by Kaasalainen et al. (2004), with axis ratios 2.7:1.1:1, and Ivar is among the most elongated NEAs whose shape is known. We have determined the rotation period of Ivar to be $4.7951689 \pm 0.0000026 \text{ h}$ with an ecliptic pole located at $336^\circ, +37^\circ \pm 6^\circ$ by incorporating lightcurves that span over 30 years. The CW spectra show Ivar to have an average OC radar albedo of 0.13 ± 0.02 , which is close to the average for S-type asteroids. The optimum bulk density is approximately 2450 kg m^{-3} and is consistent with the measured bulk density values of other S-type asteroids. We find that Ivar's spin and shape dynamics are stable.

In combination with our near-IR observations, this new shape model is currently being used to create a detailed thermophysical model of Ivar, which we will then use to study surface properties of the asteroid (Crowell et al., 2016). By using detailed shape models such as the one presented here, we are able to characterize

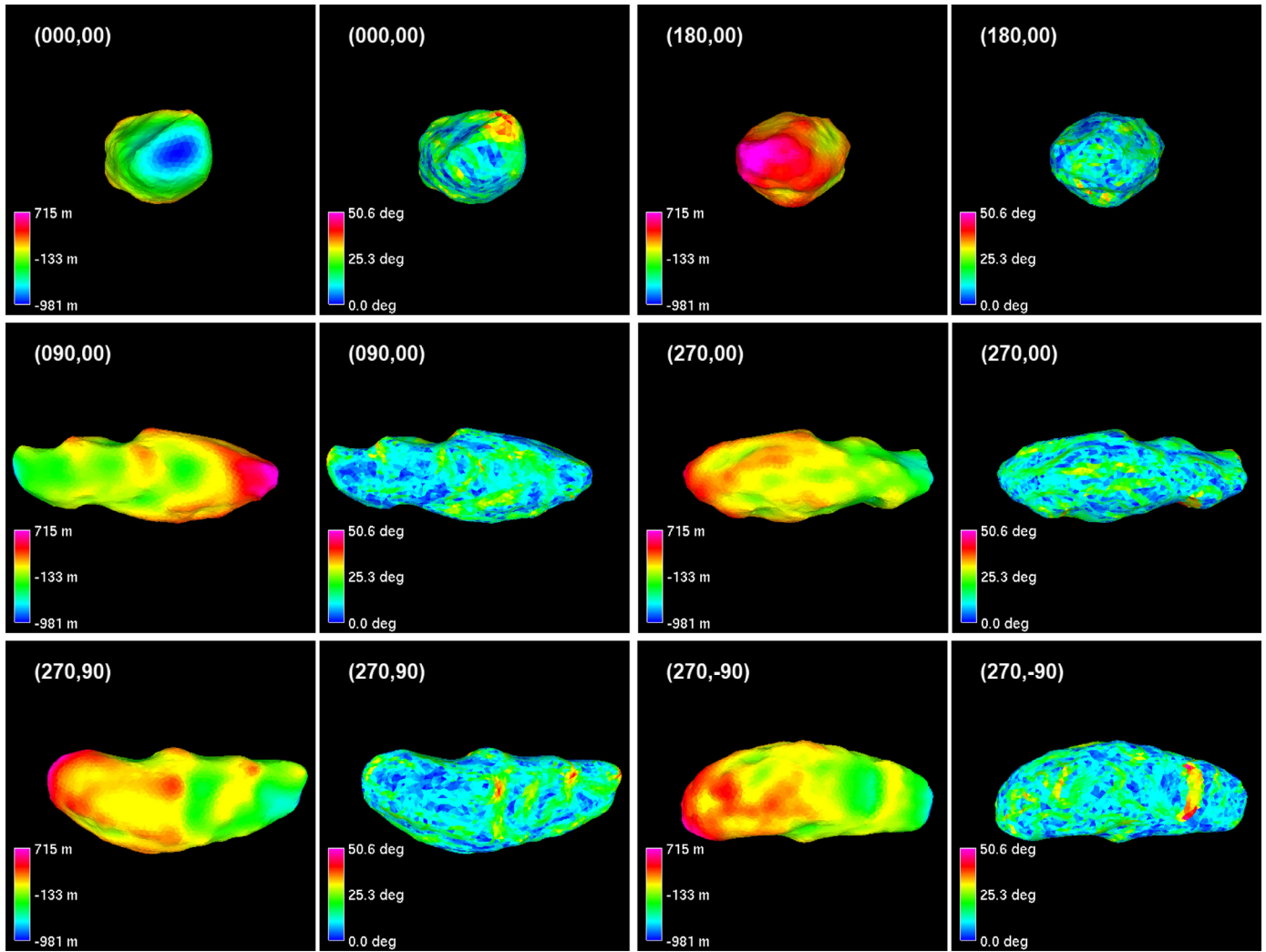


Fig. 18. The shape-model of Ivar color-coded according to dynamic elevation (left panel in each pair) and surface slope (right panel in each pair). The top row shows the two ends of the major, a-axis; the middle row shows the two ends of the b-axis; and the bottom row shows the two ends of the minor, c-axis (polar views). The maximum elevation point is located at 163° E. longitude, 3° N. latitude (at one end of the body), while the minimum elevation point is located at 354° E. longitude, 17° S latitude (the dimple in the southern hemisphere).

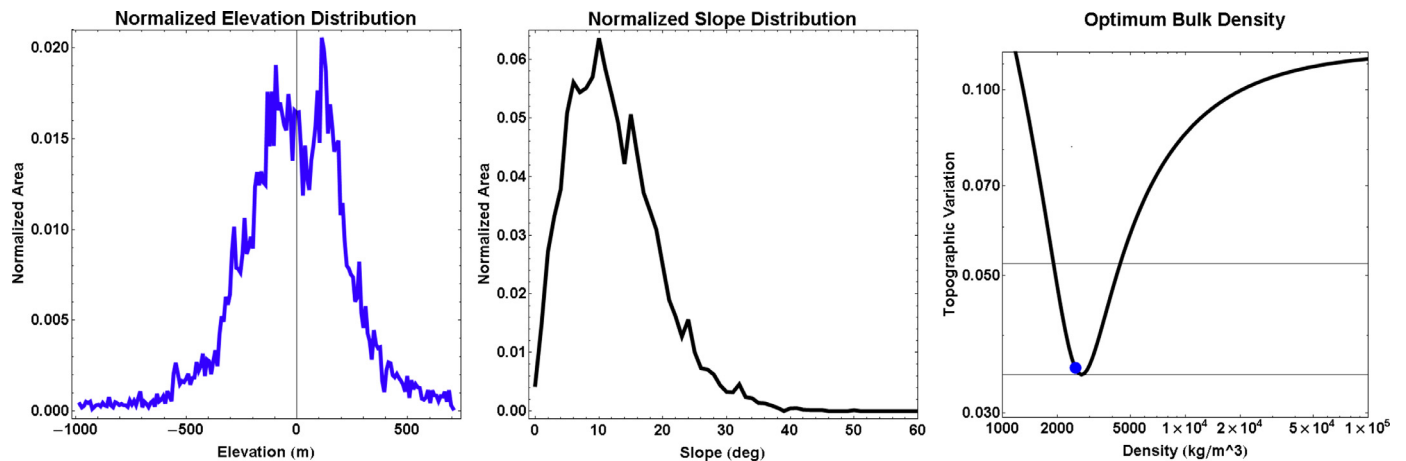


Fig. 19. (left panel) The normalized distribution of elevations over the surface of the Ivar shape model, showing a broad peak at between ± 200 m. (middle panel) The normalized distribution of slopes over the surface of the shape model, at a resolution of one facet, or about 250 m. The very low slope distribution is indicative of loose, non-cohesive materials. (right panel) The topographic variation curve for the shape-model of Ivar, generated by holding the rotation period constant at 4.7952 h and varying the bulk density of the shape. Elevation extremes, surface slopes, and surface erosion rates are minimized at an 'optimum bulk density' of $\rho = 2450$ (1700–4100) kg m^{-3} , consistent with Ivar's spectral class. Note that this is not a density measurement, but simply an indicator of the current state of the asteroid's surface.

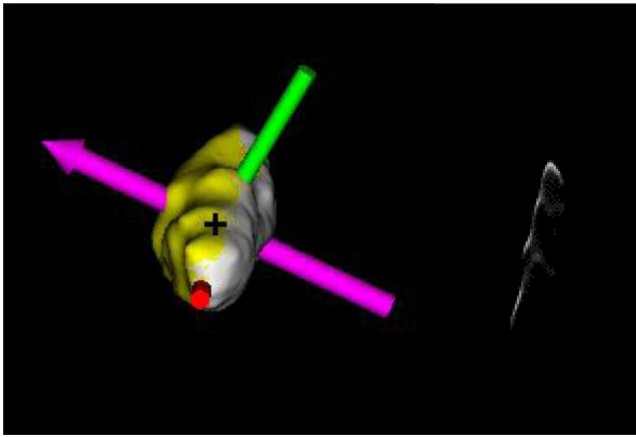


Fig. 20. We show a sky view in the same format as is shown in Fig. 10 (left) and a synthetic delay-Doppler image (right) of what we may observe in 2018. The yellow region shows the portions of Ivar that were unseen in the 2013 delay-Doppler observations. (For interpretation of the references to colour in this figure legend, the reader is referred to the web version of this article.)

surface properties and link these observations to specific regions on the asteroid's surface enabling a thorough analysis of surface heterogeneity. These results will be compared with studies for other S-complex NEAs.

Ivar's next close approach is in 2018 and will provide another opportunity for Arecibo Observatory to collect radar observations at a minimum distance of 0.31 AU. This observation window would have a 25% stronger SNR than the 2013 data. Ivar will likely not be detectable for Goldstone Observatory with a minimum distance of 0.28 AU. During this observing window, portions of Ivar that have not yet been observed with radar will be visible, allowing us to improve the model even further. In Fig. 20, we give a prediction of what we might observe from Arecibo Observatory in 2018. These observations will give us an end-on view as well as show features from the side of Ivar that was unseen in these 2015 delay-Doppler images. We will also be able to use the existing shape model to generate predictions for the 2018 apparition and compare those predictions to the actual observations as a test of our modeling efforts.

Acknowledgments

We would like to thank those who took radar observations for this project: D. Padilla, V. Negrón, W. Portalatin, and N. Despiou as well as the technicians supporting Arecibo Observatory. We would also like to thank our two anonymous reviewers who provided helpful comments and suggestions for this paper. This work was partially supported by: NSF (AST-1109855), NASA (NNX13AQ46G), and CLASS (NNA14AB05A).

Supplementary materials

Supplementary material associated with this article can be found, in the online version, at doi:10.1016/j.icarus.2016.11.008.

References

Abe, S., Mukai, T., Hirata, N., Barnouin-Jha, O.S., Cheng, A.F., Demura, H., Gaskell, R.W., Hashimoto, T., Hiraoka, K., Honda, T., Kubota, T., Matsuoka, M., Mizuno, T., Nakamura, R., Scheeres, D.J., Yoshikawa, M., 2006. Mass and local topography measurements of itokawa by hayabusa. *Science* 312, 1344–1349.

Britt, D.T., Yeomans, D., Housen, K., Consolmagno, G., 2002. Asteroid density, porosity, and structure. *Asteroids III* 485–500.

Chernova, G.P., Kiselev, N.N., 1992. Photometry of amor asteroids 1036 ganymede and 1627 ivar. *Astron. J.* 110 (4), 1875–1878.

Crowell, J.L., Howell, E.S., Magri, C., Fernandez, Y.R., Marshall, S.E., Warner, B.D., Vervack Jr, R.J., 2015. Thermophysical model of 1627 ivar. *TherMoPS II Meeting* (abstract).

Crowell, J.L., Howell, E.S., Magri, C., Fernandez, Y.R., Marshall, S.E., Warner, B.D., Vervack Jr, R.J., 2016. Thermophysical model of S-complex NEAs: 1627 ivar. *Amer. Astron. Soc., AAS Meeting #227* (abstract).

Delbo, M., Harris, A.W., Binzel, R.P., Pravec, P., Davies, J.K., 2003. Keck observations of near-Earth asteroids in the thermal infrared. *Icarus* 166, 116–130.

DeMeo, F.E., Binzel, R.P., Slivan, S.M., Bus, S.J., 2009. An extension of the bus asteroid taxonomy into the near-infrared. *Icarus* 202, 160–180.

Durech, J., Sidorin, V., Kaasalainen, M., 2010. *DAMIT: a database of asteroid models*. *A&A* 513, A46.

Hahn, G., Magnussin, P., Harris, A.W., Young, J.W., Belkora, L.A., Fico, N.J., Lupishko, D.F., Shevchenko, V.G., Velichko, F.P., Burchi, R., Ciuni, G., 1989. Physical studies of Apollo-amor asteroids: UBVR photometry of 1036 ganymede and 1627 ivar. *Icarus* 78 (2), 363–381.

Harris, A.W., Young, J.W., 1986. Photometric results for Earth-approaching asteroids. *Bull. Amer. Astron. Soc.* 17, 726.

Hoffmann, M., Geyer, E.H., 1990. Observations of asteroid 1627 ivar. *Astronomische Gesellschaft* 5 48 (abstract).

Howell, E.S., Magri, C., Vervack Jr, R.J., Fernandez, Y.R., Nolan, M.C., Taylor, P.A., Marshall, S.E., Crowell, J.L., 2015. SHERMAN: a shape-based thermophysical model for near-Earth asteroids. *American Astron. Soc., #47 Division for Planetary Sciences Meeting* (abstract).

Howell, E.S., Vervack, R.J. Jr, Magri, C., Nolan, M.C., Taylor, P.A., Fernandez, Y.R., Hicks, M.D., Somers, J.M., Rivkin, A.S., Marshall, S.E., Crowell, J.L., 2016. SHERMAN: a shape-based thermophysical model. II. Application to (8567) 1996 HW1. *Icarus*, in progress.

Huang, J., Ji, J., Ye, P., Wang, X., Yan, J., Meng, L., Wang, S., Li, C., Li, Y., Oiao, D., Zhao, W., Zhao, Y., Zhang, T., Liu, P., Jiang, Y., Rao, W., Li, S., Huang, C., Ip, W., Hu, S., Zhu, M., Yu, L., Zou, Y., Tang, X., Li, J., Zhao, H., Huang, H., Jiang, X., Bai, J., 2013. The ginger-shaped asteroid 4179 Toutatis: new observations from a successful flyby of Cheng'e-2. *Nat. Sci. Rep.* 3, 3411.

Hudson, R.S., 1994. Three-dimensional reconstruction of asteroids from radar observations. *Remote Sensing Rev.* 8 (1–3), 195–203.

Hudson, R.S., Ostro, S.J., 1994. Shape of asteroid 4769 castalia (1989 PB) from inversion of radar images. *Science* 263, 940–943.

Hudson, R.S., Ostro, S.J., 1999. Physical model of asteroid 1620 geographos from radar and optical data. *Icarus* 140, 369–378.

Kaasalainen, M., Pravec, P., Vervack, Y., Sarounova, L., Torppa, J., Virtanen, J., Kaasalainen, S., Erikson, A., Nathues, A., Durech, J., Wolf, M., Lagerros, J.S.V., Lindgren, M., Lagerkvist, C., Koff, R., Davies, J., Mann, R., Kusnirak, P., Gaftonyuk, N.M., Shervchenko, V.G., Chiorni, V.G., Belskaya, I.N., 2004. Photometry and models of eight near-Earth asteroids. *Icarus* 167, 178–196.

Magri, C., Ostro, S., Sheeres, D., Nolan, M.C., Giorgini, J.D., Benner, L.A.M., Margot, J., 2007. Radar observations and a physical model of asteroid 1580 betulia. *Icarus* 186, 152–177.

Magri, C., Howell, E.S., Nolan, M.C., Taylor, P.A., Fernandez, Y.R., Mueller, M., Vervack Jr, R.J., Benner, L.A.M., Giorgini, J.D., Ostro, S.J., Scheeres, D.J., Hicks, M.D., Rhoades, H., Somers, J.M., Gaftonyuk, N.M., Kouprianov, V.V., Krugly, Y.N., Molotov, I.E., Busch, M.W., Margot, J., Benishek, V., Protitch-Benishek, V., Galad, A., Higgins, D., Kusnirak, P., Pray, D.P., 2011. Radar and photometric observations and shape modeling of contact binary near-Earth asteroid (8567) 1996 HW1. *Icarus* 214, 210–227.

Mainzer, A., Bauer, J., Cutri, R.M., Grav, T., Masiero, J., Beck, R., Clarkson, P., Conrow, T., Dailey, J., Eisenhardt, P., Fabinsky, B., Fajardo-Acosta, S., Fowler, J., Gelino, C., Grillmair, C., Heinrichsen, I., Kendall, M., Kirkpatrick, J.D., Liu, F., Masci, F., McCallon, H., Nugent, C.R., Papin, M., Rice, E., Royer, D., Ryan, T., Sevilla, P., Sonnett, S., Stevenson, R., Thompson, D.B., Wheelock, S., Wiemer, D., Wittman, M., Wright, E., Yan, L., 2014. Initial performance of the NEOWISE reactivation mission. *Astron. J.* 792, 30.

Mitchell, D.L., Ostro, S.J., Hudson, R.S., Rosema, K.D., Campbell, D.B., Velez, R., Chandler, J.F., Shapiro, I.I., Giorgini, J.D., Yeomans, D.K., 1996. Radar observations of asteroids 1 Ceres, 2 Pallas, and 4 vesta. *Icarus* 124, 113–133.

Nolan, M.C., Magri, C., Howell, E.S., Benner, L.A.M., Giorgini, J.D., Hergenrother, C.W., Hudson, R.S., Lauretta, D.S., Margot, J., Ostro, S.J., Scheeres, D.J., 2013. Shape model and surface properties of the OSIRIS-Rex target asteroid (101955) bennu from radar and lightcurve observations. *Icarus* 226, 629–640.

Ostro, S.J., Campbell, D.B., Hine, A.A., Shapiro, I.I., Chandler, J.F., Werner, C.L., Rosema, K.D., 1990. Radar images of asteroid 1627 ivar. *Astron. J.* 99 (6), 2012–2018.

Pravec, P., Sarounova, L., Wolf, M., 1996. Lightcurves of 7 near-Earth asteroids. *Icarus* 124 (2), 471–482.

Rayner, J.T., Toomey, D.W., Onaka, P.M., Denault, A.J., Stahlberger, W.E., Vacca, W.D., Cushing, M.C., Wang, S., 2003. SpeX: a medium-resolution 0.85–5.5 μ spectrograph and imager for the NASA infrared telescope facility. *Publ. Astron. Soc. Pacific* 115, 362–382.

Richardson, J.E., Melosh, H.J., Greenberg, R., 2004. Impact-induced seismic activity on asteroid 433 Eros: a surface modification process. *Science* 306, 1526–1529.

Richardson, J.E., Melosh, H.J., Greenberg, R.J., O'Brien, D.P., 2005. The global effects of impact-induced seismic activity on fractured asteroid surface morphology. *Icarus* 179, 325–349.

Richardson, J.E., Melosh, H.J., Lisse, C.M., Carcich, B., 2007. A ballistics analysis of the deep impact ejecta plume: determining comet tempel 1's gravity, mass, and density. *Icarus* 190, 357–390.

- Richardson, J.E., Bowling, T.J., 2014. Investigating the combined effects of shape, density, and rotation on small body surface slopes and erosion rates. *Icarus* 234, 53–65.
- Skiff, B.A., Bowell, E., Koehn, B.W., Sanborn, J.J., McLelland, K.P., Warner, B.D., 2012. Lowell observatory near-Earth asteroid photometric survey (NEAPS) – 2008 May through 2008 december. *Minor Planets Bull.* 39-3, 111–130 (ISSN 1052-8091).
- Tedesco, E., Marsden, B.G., and Williams, G.V., 1990. *Minor planets circular 17249-17472*, 17262.
- Thomas, P.C., Belton, M.J.S., Carcich, B., Chapman, C.R., Davies, M.E., Sullivan, R., Veverka, J., 1996. The shape of ida. *Icarus* 120, 30–32.
- Warner, B.D., 2014. Near-Earth asteroid lightcurve analysis at CS3-Palmer divide Station: 2013 june-september. *Minor Planet Bull.* 41-1, 41–47 (ISSN 1052-8091).
- Warner, B.D., 2015. Near-Earth asteroid lightcurve analysis at CS3-Palmer divide Station: 2015 january-march. *Minor Planet Bull.* 42-3, 172–183 (ISSN 1052-8091).
- Werner, R.A., 1994. The gravitational potential of a homogeneous polyhedron or don't cut corners. *Celestial Mech. Dyn. Astronomy* 59, 253–278.
- Virkki, A., Muinonen, K., Penttilä, A., 2014. Inferring asteroid surface properties from radar albedos and circular-polarization ratios. *Meteor. Planet. Sci.* 49 (Nr 1), 86–94.
- Yeomans, D.K., Antreasian, P.G., Barriot, J.P., Chesley, S.R., Dunham, D.W., Farquhar, R.W., Giorgini, J.D., Helfrich, C.E., Konopliv, A.S., McAdams, J.V., Miller, J.K., Owen, W.M., Scheeres, D.J., Thomas, P.C., Veverka, J., Williams, B.G., 2000. Radio science results during the NEAR-Shoemaker spacecraft rendezvous with eros. *Science* 289, 2085–2088.